ORIGINAL ARTICLE

Preparation of Ag@Ag$_2$O/AgCl composite photocatalytic material and degradation performance for SD I under sunlight

Daxiang Gao[1]

Abstract

The photocatalytic material Ag@Ag$_2$O/AgCl was successfully prepared using GO and CA gel as carriers, through chemical coupling, in situ deposition, and photo-induced reduction. The performance of the composite photocatalytic material, its photodegradation performance, mechanism, and pathways of Sudan I (SD I) in APG aqueous solution were explored. The results showed that the prepared composite photocatalytic material was loaded with a large amount of irregular nano-Ag$_2$O, AgCl, and silver nanoparticles (AgNPs). In the material, the mass fraction of Ag element is the highest (36.41 wt%). The photocatalytic material showed a significant broad absorption in both the UV and visible light regions, and under visible light irradiation, it can generate a stable and reversible photocurrent, with a small resistance to photogenerated electron transfer, exhibiting good photocatalytic performance. SD I exhibits good solubility in APG (7 mL/1000 mL) aqueous solution after ultrasonic and heating (100 $^{\circ}$C) treatment for 30 min. At a certain concentration of SD I, acidic solution and lower temperature are conducive to the photocatalytic degradation of SD I, and the catalytic degradation process conforms to the pseudo-first-order reaction kinetic relationship. Through five cycles of experiments, the stability of the material was demonstrated to be good. Superoxide radicals ($\cdot O_2^-$) and holes (h$^+$) generated during the photocatalytic degradation are the main active species responsible for degrading SD I. SD I molecules were decolorized by N=N and C-N bond cleavage, and the benzene and naphthalene ring were opened under the action of active substances (h$^+$, $\cdot O_2^-$) and finally mineralized into CO$_2$, H$_2$O and inorganic ions.

Keywords Sudan I · Ag@Ag$_2$O/AgCl · Alkyl polyglucoside (APG) · Photocatalysis · Graphene oxide · Sodium alginate

Introduction

Sudan are synthetic lipophilic azo compounds, with Sudan II, III, and IV all being derivatives of Sudan I (Sudan I, abbreviated as SD I, 1-phenylazo-2-naphthol). Sudan are generally insoluble in water, but easily soluble in organic solvents, mainly used in petroleum, lubricating oil and other industrial solvents (Khan et al. 2020). SD I is classified as a third-class carcinogen, and its adduct generated with the DNA of animals can cause tumors in the bladder, spleen, liver, and other organs (Eteng et al. 2021). Currently, the degradation methods of Sudan mainly include microbial degradation (Pan et al. 2011), electrochemical treatment

(Qi et al. 2015), and photocatalysis (Liu et al. 2009; Li et al. 2020a). When traditional microbial treatment technology is used to treat Sudan, intermediate product aniline will be produced, which is still toxic and harmful to the environment. The high cost of electrochemical treatment makes practical application difficult. In related studies, simulated wastewater was prepared using anhydrous ethanol with 20 g/L NaCl (Qi et al. 2015), or an aqueous solution of SD I was obtained by mixing the acetonitrile solution of SD I with distilled water in a 2:8 ratio (Zhang 2009). Although these organic solvents are relatively easy to dissolve Sudan under experimental conditions, they are difficult to promote in practical applications due to their high cost. Therefore, the solubility and effective and rapid degradation of Sudan in water system are urgent difficulties to be solved.

Recently, many semiconductor materials have been developed for photocatalytic materials, such as TiO$_2$ (Gopalan et al. 2020), Bi$_2$O$_3$ (Keshavulu et al. 2023), ZnO (Keshavulu et al. 2024), and NaLaTi$_2$O$_6$ (Ramesh et al. 2018). TiO$_2$, as

✉ Daxiang Gao
1183772425@qq.com

1 Biological Engineering Technology Center, Jiangsu Vocational College of Agriculture and Forestry, Jurong 212400, China

the most representative semiconductor photocatalyst, possesses advantages such as high chemical stability, non-toxicity, and low cost. However, since TiO_2 is a wide bandgap semiconductor (3.2 eV), it can only absorb UV light, resulting in a low utilization rate of solar energy (Gu et al. 2022). Silver salts exhibit high activity in visible light, as Ag^+ has the electron configuration of d10, which favors the enhancement the photocatalytic activity of the corresponding material. Therefore, Ag-based photocatalysts have received extensive study in hydrogen production or degradation of organic wastewater (Yang et al. 2023; Sun et al. 2020). For example, Ag_2O is an efficient photocatalyst with a narrow band gap (1.2 eV), good photocatalytic performance, and high visible light absorption. However, the photochemical stability of silver-based semiconductor materials is generally poor, leading to easy agglomeration and recombination of photogenerated electrons and holes (Zhao et al. 2019). Therefore, the construction of binary (Shi et al. 2017; Yang et al. 2016; Sun et al. 2019) or ternary heterojunctions of silver-based semiconductors (Ren et al. 2015; Qianqian et al. 2020) can effectively solve this problem. However, the specific surface area of silver-based semiconductors is generally low, with poor adsorption capacity and the powder particles are small, difficult to separate and recycle (Anqi et al. 2022). Moreover, domestic and foreign research mainly focused on visible light (Li et al. 2020b; Xiao et al. 2018), with little utilization of solar energy resources (Ghaly et al. 2017). Therefore, the construction of efficient, stable, and recyclable photocatalytic composites and the full use of solar energy resources will be the focus of future research. Sodium alginate (SA) is a natural polymer polysaccharide compound, with advantages such as biodegradability, stability, safety, and non-toxicity. Its oxygen-containing groups chelate with Ca^{2+} to form a calcium alginate (CA) gel with a three-dimensional network structure. CA gel has a large surface area and various active functional groups; therefore, the catalytic degradation material combined with CA gel can effectively degrade pollutants while adsorbing them (Song et al. 2013; Gao et al. 2019). Graphene oxide (GO) is a novel carbon-based material with large surface area that can rapidly adsorb organic pollutants in the system and has gained wide attention in the field of photocatalysis (Chen et al. 2013; Xiu et al. 2014).

In the preliminary experiments, it was found that under certain conditions, SD I can be directly dissolved in the aqueous solution of alkyl polyglycoside (APG) without adding other fat-soluble solvents. APG is recognized as a new generation of green surfactant in the world. It is non-toxic and can be completely biodegraded (Xiao et al. 2016). The theme of this study is the efficient degradation of SD I aqueous solution using prepared photocatalytic material under sunlight. The $Ag@Ag_2O/AgCl$ insoluble catalytic material with high photodegradation performance was constructed by chemical coupling, in situ deposition, and photo-induced reduction using GO and CA gel as carriers. The structure of the photocatalytic material was characterized, and for the first time, its photocatalytic degradation performance of SD I in APG aqueous solution under sunlight was studied in detail. This research provides new insights into constructing solvent systems for insoluble pollutants and offers a novel approach for promoting the photocatalytic degradation of Sudan dyes.

Experimental

Materials

GO (Shanghai Maoguo Nanotechnology Co., Ltd), cetyltrimethyl ammonium bromide (CTAB), SA and SD I (Xilong Chemical Co., Ltd), EDTA-2Na, tert-butyl alcohol (TBA), and p-benzoquinone (p-BQ) (West Asia Chemical Technology Co., Ltd), alkyl polyglucoside (Jiangsu Wanqi Biotechnology Co., Ltd, neutral, solid content $\geq 50\%$).

Preparation of photocatalytic material

16 mL of 10 g/L CTAB solution and 100 mL of 4 g/L SA solution were mixed together. After stirring for 10 min, 20 mL GO dispersion (2 g/L) and 12 mL $AgNO_3$ solution (50 g/L) were slowly dripped into the mixture under magnetic stirring, respectively. After stirring for 15 min, 40 mL of 30 g/L Ca $(NO_3)_2$ solution, 12 mL of 10 g/L NaCl solution, and 24 mL of 10 g/L KOH solution were slowly added to the mixed solution,respectively. The precipitate of the mixed system was dispersed in deionized water and irradiated in sunlight for 1 h under stirring. The composite photocatalytic material was obtained by filtration. 400 mL suspension was prepared with deionized water for the catalytic degradation of SD I. Part of the suspension was centrifuged and vacuum freeze-dried to obtain $Ag@Ag_2O/AgCl$ photocatalytic material for detection, labeled as material 1.

Characterization of photocatalytic material

The morphologies of the prepared photocatalytic material was analyzed with the Hitachi SU8010-type scanning electron microscope and the Japanese JEM-2100F transmission electron microscope. The optical characteristics of the material were measured using a UV-1901 UV–visible diffuse reflectance spectrometer (DRS). The chemical state of the sample was determined by using an ESCALAB250Xi X-ray photoelectron spectrometer (XPS). ESR spectra of the solution were recorded by a JES-FA200 electron paramagnetic resonance spectrometer. The photocurrent and EIS of the composite were analyzed using a CHI-660 E electrochemical

workstation from Shanghai Chenhua Instrument Co., Ltd., with a 0.05 mol·L^{-1} Na$_2$SO$_4$ solution. Ultra-high performance liquid chromatography (UPLC, 1290, Agilent, USA) and electrospray tandem mass spectrometry (ESI-MS/MS, QTOF6550, Agilent, USA) were combined to analyze SD I and its intermediates in positive ion mode.

Solubility of SD I in APG aqueous solution

0.012 g of SD I was added to 980 mL of deionized water. After ultrasonic dispersion treatment at 80 W power for 10 min, it was fetched out and placed in a stationary temperature water bath at 60 ℃. Different volumes (0–7 mL) of APG original solution were added, and the final volume of 1000 mL was supplemented with deionized water. After stirring evenly, the effects of the amount of APG on the solubility of SD I and the absorbance of the solution were observed. 0.012 g SD I was added to 1000 mL aqueous solution containing 7 mL APG original solution. After ultrasonic treatment, the solution was heated in a water bath. The solution temperature was controlled at a set value (20–100 ℃). The effects of different heating temperatures and boiling water bath (100 ℃) duration were investigated.

Photocatalytic degradation test

The 10 mL suspension of the prepared material 1 was centrifuged to obtain the material particles, and then mixed with 100 mL 10 mg/L SD I APG aqueous solution (containing 0.7 mL APG stock solution, first ultrasonic 10 min, then 100 ℃ boiling water bath for 30 min). The initial pH was adjusted to 4 with acetic acid, and the temperature was controlled at 30 ℃. After reaching adsorption equilibrium through stirring in dark for 30 min, the suspension was directly irradiated under sunlight. The experiment was carried out in sunny weather with the minimum change of solar radiation energy in a day (11: 00–13: 00). Stirring during the photocatalytic reaction was achieved using a magnetic stirrer, with samples being taken every 5 min.

The relationship between C_0/C_t and t was used to investigate the efficiency of photocatalytic degradation, and the degradation rate (η) was calculated as $\eta = [(C_0 - C_t)/C_0] \times 100\%$, where C_0 and C_t represent the SD I concentration of initial and reaction time t, respectively. The first-order degradation reaction rate equation ($\ln(C_0/C_t) = k\mathrm{t} + A$) was used to describe the kinetic liner relationship and the half-life ($T_{1/2}$) of photolysis was expressed by $\ln2/k$ (Wang et al. 2010), where k is the first-order apparent rate constant(min^{-1}). p-BQ (0.2 g), TBA (4 mL), and EDTA-2Na (0.2 g) were utilized as the scavengers of ·O$_2^-$, ·OH, and h$^+$ respectively.

Results and discussion

Characterization results of photocatalytic material

SEM and TEM results

The wrinkled structure of the prepared material is loaded with some irregularly shaped nano-Ag$_2$O, AgCl, and silver nanoparticles (AgNPs) (Fig. 1a, b). These particles are distributed in clusters, and the particle sizes are not uniform. The successful loading of Ag@Ag$_2$O/AgCl particles on the Ca^{2+} cross-linked GO/CA wrinkles can be observed. The wrinkled structure can effectively disperse the cluster-like Ag@Ag$_2$O/AgCl particles and enhancing the adsorption and degradation of pollutants by the catalytic material. Figure 1c, d clearly shows that particles of different sizes are gathered together and unevenly distributed. HRTEM (Fig. 1e) indicates that the particles are polycrystalline structure, showing the diffraction crystal planes of Ag$_2$O (111), AgCl (200) and Ag (111), with a spacing of 0.272, 0.280, and 0.240 nm, respectively. It can be seen from the SAED image (Fig. 1f) that the material exhibits an obvious polycrystalline diffraction ring.

EDS analysis

Figure 2 illustrates the EDS spectrum of the catalytic material 1 and the proportion of each element. It is evident that the prepared material 1 contains elements such as Ag, Cl, C, O, Ca, and Br, with the highest mass fraction of Ag element at 36.41 wt%, followed by C and O. The atomic mole fraction of Ag (7.70%) is second only to C and O, approximately 3 times that of Cl atoms, i.e., Ag (or Ag$_2$O): AgCl = 2: 1, indicating the presence of nano-Ag$_2$O and AgNPs in material 1 in addition to AgCl. Furthermore, the material contains slight amount of Br element in the form of AgBr particles, which can also synergistically catalyze the degradation of SD I along with Ag@Ag$_2$O/AgCl.

The distribution maps of Ag, Cl and other elements are obtained in Fig. 3. The Ag element is unevenly distributed, similar to the Cl element, showing the uneven distribution of AgCl, but without the phenomenon of large-scale aggregation.

XPS results

The XPS analysis results of material 1 are shown in Fig. 5 and Table 1. The elements C, O, Ag, Cl, and Ca are observed in Fig. 4a, showing the material 1 is composed of these elements. In Fig. 4b, the two peaks of Ag $3d$ are deconvoluted into four peaks at 367.34, 368.22, 373.34, and 374.22 eV,
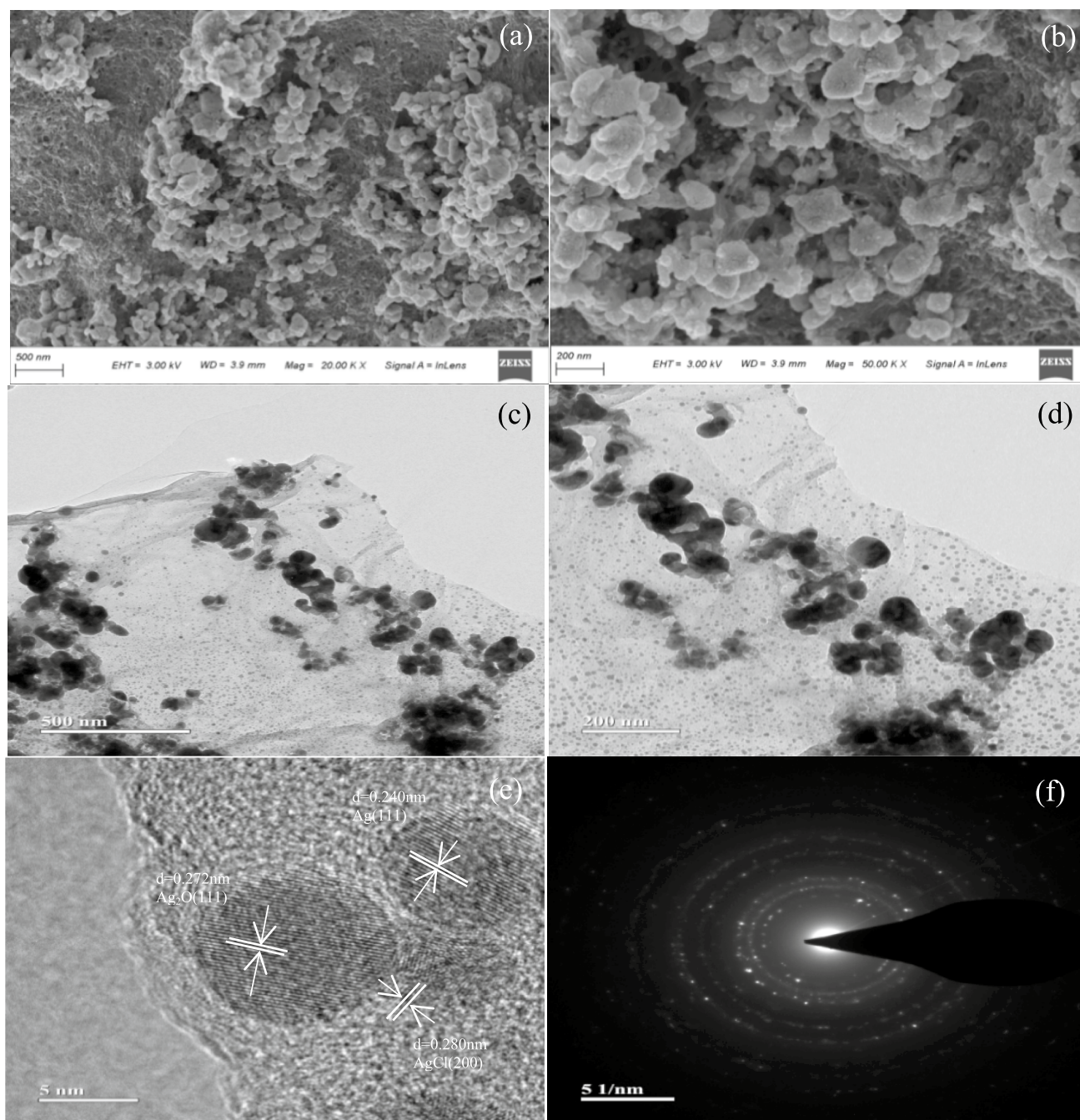
Fig. 1 SEM (**a**, **b**), TEM (**c**, **d**), HRTEM (**e**), and SAED (**f**) images of the prepared material 1

which are attributed to the Ag $3d_{5/2}$ and Ag $3d_{3/2}$. The peaks at 367.34 and 373.34 eV could be attributed to the Ag$^+$ of the AgCl (or Ag$_2$O), the peaks at 368.22 and 374.22 eV could be ascribed to Ag^0 (Shi et al. 2013). This result confirms the presence of Ag and Ag$^+$ in the material, indicating that Ag$^+$ is partially converted to Ag after irradiation. It is consistent with the XRD analysis conclusion. In Fig. 4c, three peaks of C 1 *s* at 284.80, 286.22, and 287.74 eV that correspond to the C=C/C–C, C–O, and C=O, respectively

(Gao et al. 2015). We can observe two peaks at 198.14 and 199.78 eV in the XPS pattern of Cl 2*p* (Fig. 4d), which could be attributed to Cl $2p_{3/2}$ and Cl $2p_{1/2}$, respectively.

In Fig. 4e, three obvious oxygen signals are observed at 530.69, 532.10, and 533.23 eV, corresponding to surface lattice oxygen (metal and oxygen bonding, labeled as O$_L$), oxygen vacancy (labeled as O$_V$), and adsorbed oxygen (labeled as O$_H$), respectively (Xia et al. 2014), with proportions of 33.24%, 57.28%, and 9.48%, respectively.

Fig. 2 EDS spectrum and proportion of each element of the material 1

Element	Weight/%	At/%
C	35.90	68.16
O	11.41	16.26
Cl	4.06	2.61
Ag	36.41	7.70
Ca	6.25	3.57
Br	5.98	1.71
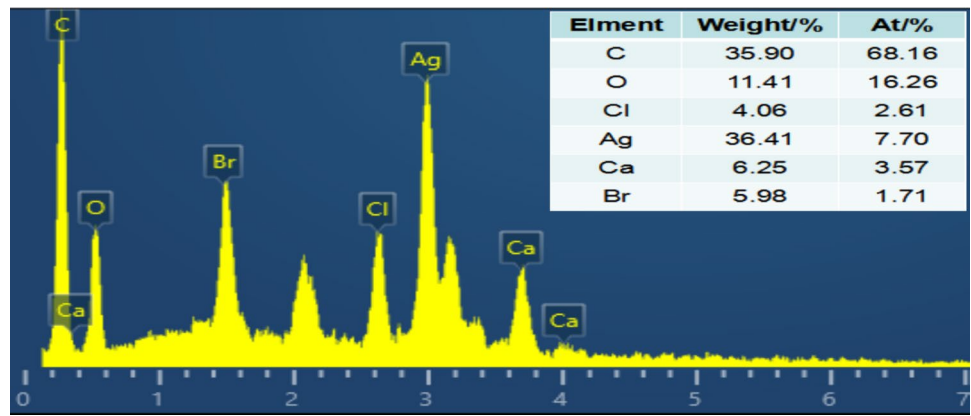
Fig. 3 Element distribution maps of the material 1
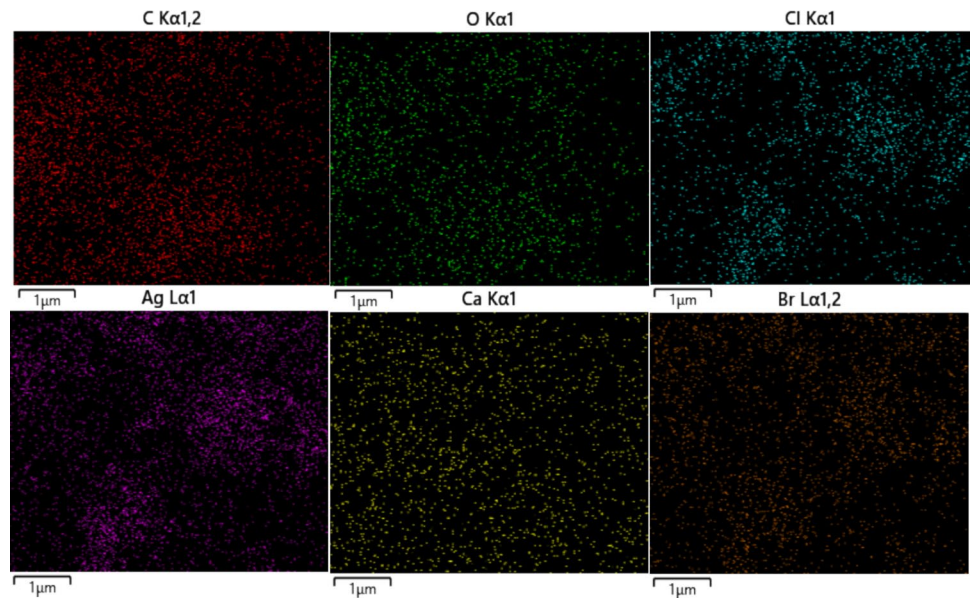
Table 1 XPS peak separation of the material 1

Element	Name	Peak BE/eV	FWHM/eV	Area (P) CPS/eV	Atomic/%
C 1s	C–C	284.80	1.42	50915.97	54.18
	C–O	286.22	1.32	24982.84	26.61
	C=O	287.74	2.18	18023.4	19.21
O 1s	O_L	530.69	2.01	31174.15	33.24
	O_V	532.10	1.71	53659.69	57.28
	O_H	533.23	2.7	8873.15	9.48
Ag 3d	$Ag^+ 3d_{5/2}$	367.34	1.83	6143.88	5.66
	$Ag^+ 3d_{3/2}$	373.34	1.52	3537.02	
	$Ag^0 3d_{5/2}$	368.22	1.11	60380.44	94.34
	$Ag^0 3d_{3/2}$	374.22	1.11	41528.59	
Cl 2p	$Cl^- 2p_{3/2}$	198.14	1.17	5201.95	100
	$Cl^- 2p_{1/2}$	199.78	1.17	2616.65	

The lattice oxygen peak at 530.69 eV belongs to Ag_2O. The broad peak at 533.23 eV suggests the presence of multiple oxygen ions, which could be surface hydroxyl groups or oxygen adsorbed from H_2O, as the material was prepared in an aqueous solution, or it could be carbonate species. The formation of carbonates is caused by
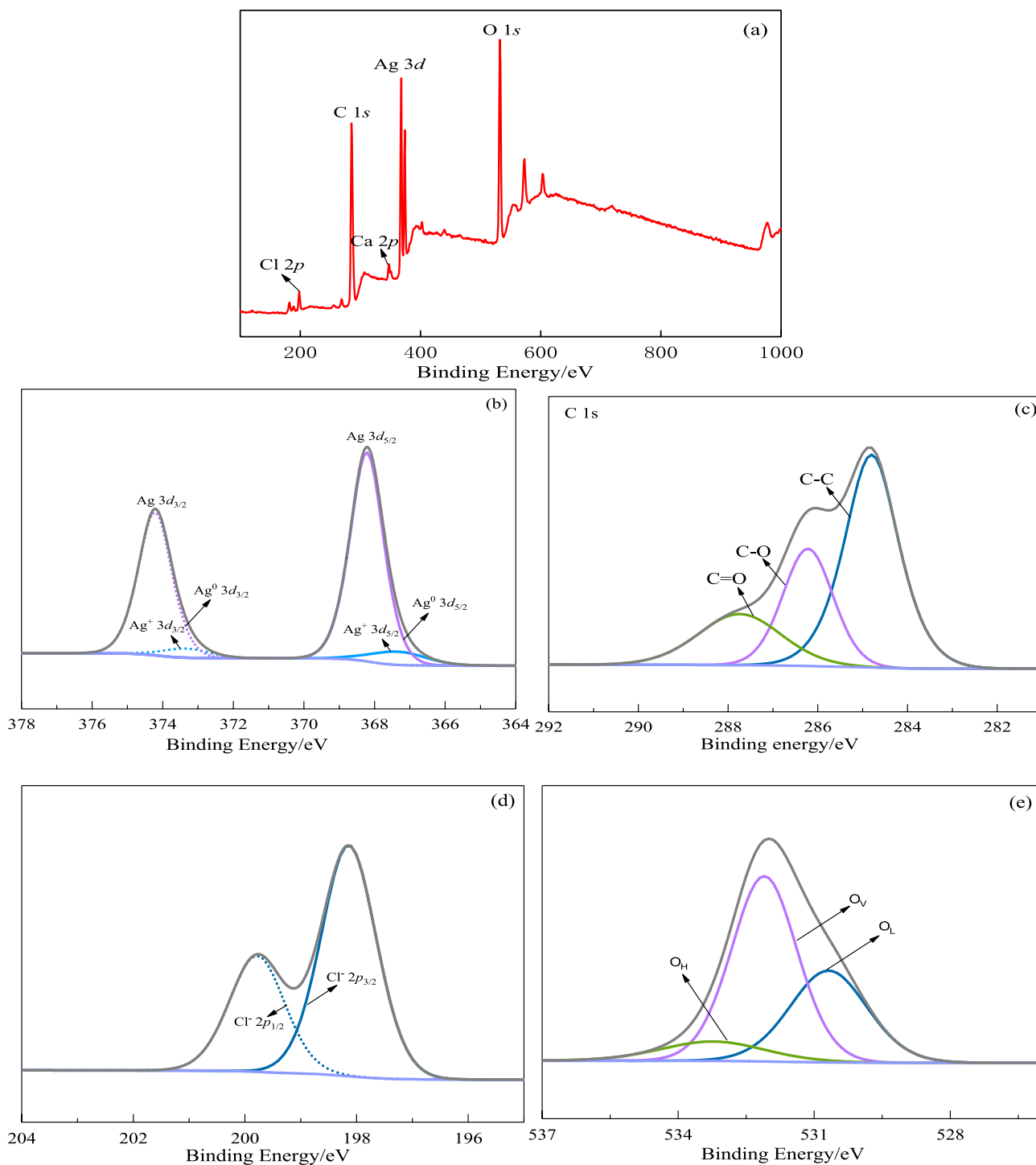
Fig. 4 XPS spectra of the material 1: survey spectrum (**a**), Ag 3*d* (**b**), C 1 *s* (**c**), Cl 2*p* (**d**), and O 1 *s* (**e**)

the reaction of surface oxygen atoms with atmospheric CO_2, which is a common phenomenon in all silver oxides (Waterhouse et al. 2007). Among the three oxygen species, lattice oxygen is beneficial to the partial oxidation of SD I, while adsorbed oxygen related to oxygen vacancy or low-coordinated surface molecular oxygen favors the complete oxidation of SD I (Ghaly et al. 2017). It is generally believed that surface oxygen vacancies are ideal surface defects for enhancing light absorption, separation, and transfer of photogenerated carriers in catalytic materials, thereby exhibiting high photocatalytic efficiency (Qin et al. 2018).
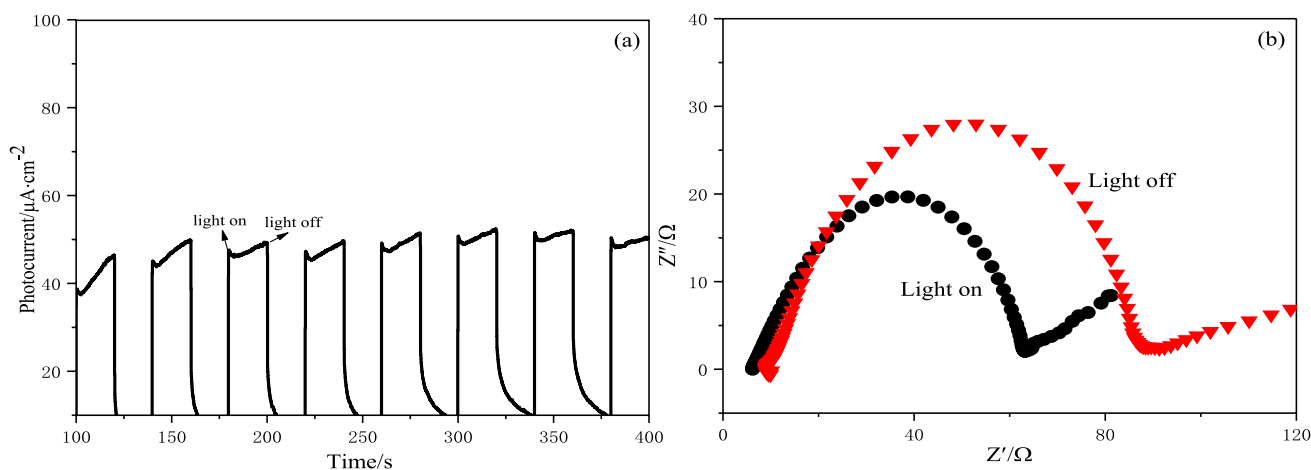
Fig. 5 The photocurrent (**a**) and EIS (**b**) of the material 1

Electrochemical properties

As shown in Fig. 5a, the material exhibited no photocurrent response in dark condition, but under visible light irradiation, it generated stable photocurrent, showing good reversibility. Compared with that in the dark, the prepared photocatalytic material has small photoactive electron transfer resistance under visible light irradiation and show good photocatalytic properties (Fig. 5b).

The band gap energy of pure AgCl tends to be large (~ 3.25 eV) (Li et al. 2017), which can only absorb and utilize UV light. In contrast, the narrow band gap (1.2 eV) of Ag_2O and the SPR effect of AgNPs can significantly enhance the absorption of the catalytic material in the visible and infrared regions. By adjusting the content of AgCl in the composite material and introducing Ag_2O and Ag, the photocatalytic performance can be achieved, which is of

positive significance for the material to make better use of the visible and infrared light in solar energy.

UV–vis DRS

In Fig. 6a, pure GO primarily absorbs light in the UV region, while SA shows no absorption. The photocatalytic material 1 exhibits significant absorption in both the UV and visible light regions, with no distinct absorption edge, indicating a broad absorption range. AgCl has a wide band gap and can only use UV light, while Ag_2O can use visible light, but its band gap is narrow, which is prone to rapid recombination of photogenerated carriers. The photocatalytic material formed after compounding contain AgNPs, Ag_2O, and AgCl, resulting in strong absorption bands from UV to near-infrared regions, and the band gap of the photocatalytic material (1.5 eV) is enhanced (Fig. 6b), reducing the chances of rapid
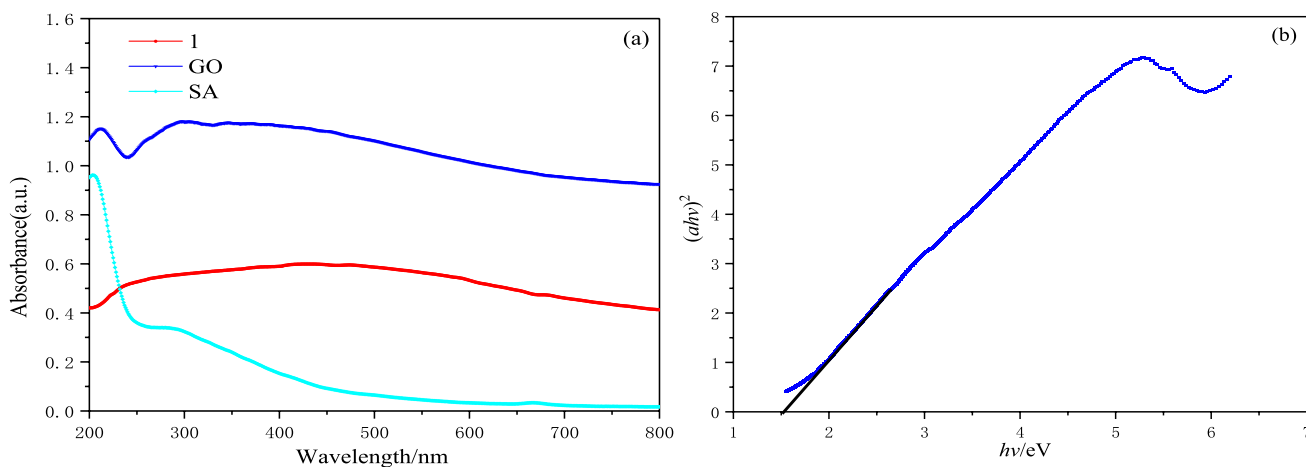

Fig. 6 UV–vis spectra (**a**) of the material 1 and the plot (**b**) of $(\alpha h v)^2$ versus energy$(h v)$

recombination of photogenerated carriers. Furthermore, GO possesses excellent high electron mobility, abundant adsorption sites, and a high specific surface area (Bi et al. 2011), making a small amount of GO effective in enhancing the light absorption capacity of the material.

Solubility of SD I in APG solution

SD I forms a conjugated system through azo bonds, with its absorption peak located in the visible light region, while the absorption peaks of naphthalene and phenyl structures are found in the UV light region (Zhang et al. 2023). In Fig. 7a, b, due to the insolubility of SD I in water, no distinct characteristic absorption peaks were observed in its suspension. As the amount of APG added increased, characteristic peaks of SD I appeared in the APG aqueous solution, primarily located at 224, 305, and 484 nm. The absorption peak at 224 nm corresponds to the phenyl structure, the peak at 305 nm is a weak absorption peak resulting from the $n \rightarrow \sigma*$ transition of the naphthalene ring occurring in the near-ultraviolet region, while the characteristic absorption peak at 484 nm in the visible light region is caused by the azo

conjugated system. With the increase in the amount of APG added, the absorption peak at 484 nm significantly intensified, indicating an increase in the solubility of SD I. Since the absorption peak at 484 nm is unaffected by APG, it can serve as a basis for assessing the solubility of SD I and the photocatalytic degradation of SD I. The best solubility effect was observed when the amount of APG added was 7 mL.

Figure 7c shows that the heating temperature has a significant effect on the dissolution rate of SD I. The dissolution rate of SD I is slow below 40 ℃, while above 40 ℃, the dissolution rate is accelerated, resulting in a significant change in the absorbance near 484 nm. In addition, with the increase of temperature, the absorption peak position in the visible light region slightly blue shifted from 484 nm (20–40 ℃) to 481 nm (80–100 ℃), which may be due to the increase of the amount of SD I dissolved, resulting in more intramolecular hydrogen bonds formed, reducing π bond delocalization range (Cao et al. 2011). Therefore, it is more appropriate to choose the heating temperature of 100 ℃. As shown in Fig. 7d, the absorbance reached the maximum after heating for 30 min and then decreased, which may be due to the large hydrophobic group of SD I, resulting in the
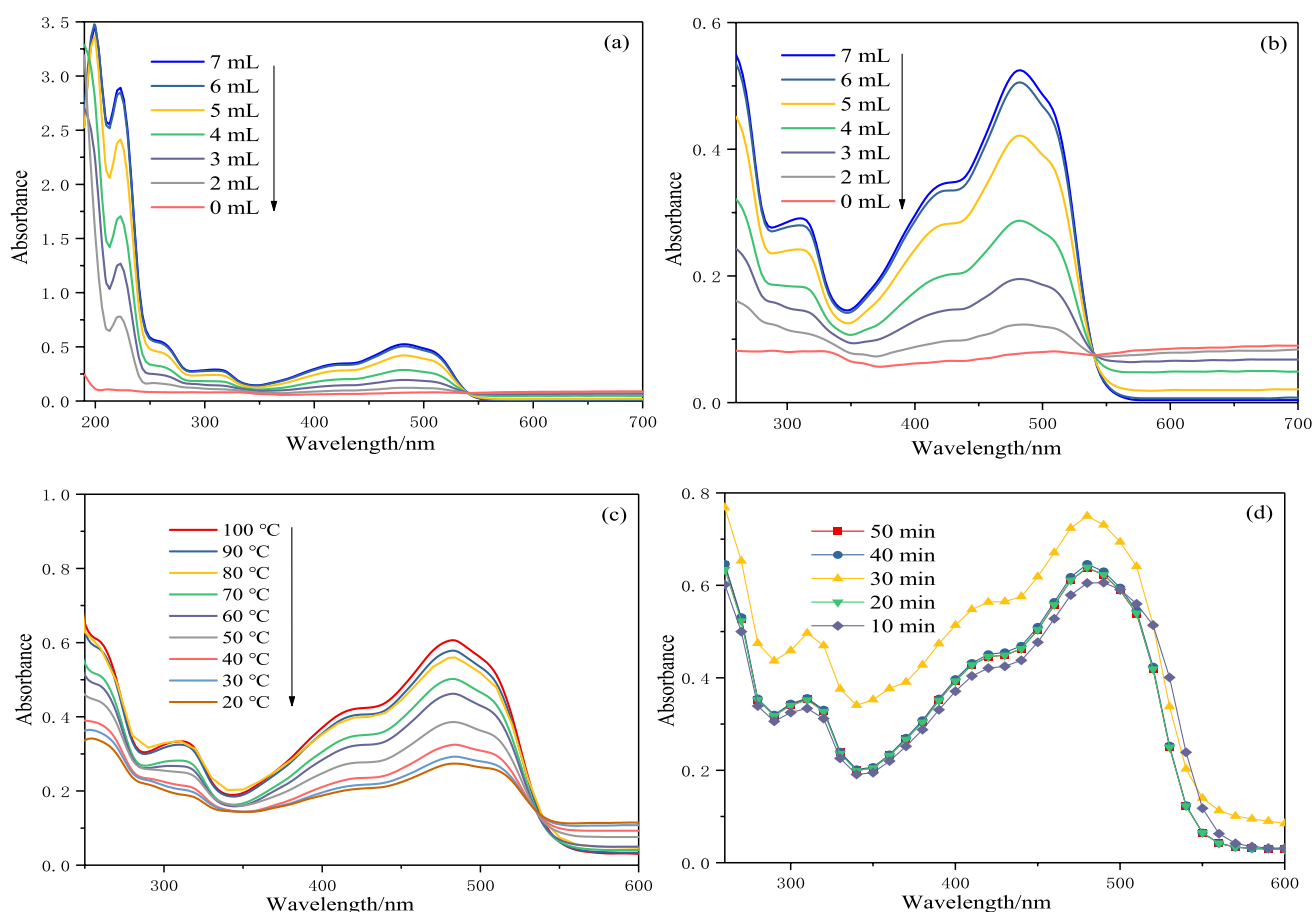

Fig. 7 Factors affecting the solubility of SD I: APG concentrations (**a**, **b**), different temperatures (**c**), and different heating time at 100 ℃ (**d**)

gradual precipitation of some SD I from APG aqueous solution. Therefore, heating for 30 min is the optimal choice.

Influencing factors of photocatalytic degradation

Effect of pH value

Preliminary experiments found that after 60 min of visible light irradiation, there was almost no degradation of SD I in the blank experiment (without catalyst), indicating that the self-degradation of SD I within 60 min can be negligible. The photocatalytic degradation of SD I accelerates with the continuous decrease in wastewater pH. The highest degradation efficiency of SD I occurred at pH 5 within the pH range of 5–9 (Fig. 8a). When the pH value is greater than 6, after 30 min of photocatalytic degradation, a characteristic absorption peak of AgNPs is detected in the range of 400–430 nm. This is due to the particles' surface being

susceptible to corrosion under sunlight in neutral and alkaline solutions, leading to partial conversion of the original AgCl into AgNPs (Fig. 8b). The presence of AgNPs in the solution deepens its color and influences the photocatalytic reaction.

The stronger the acidity of the solution, the faster the degradation rate of SD I (Fig. 9). The photocatalytic degradation reactions all follow pseudo-first-order kinetics. Further calculations reveal that at 20 ℃, the k for the degradation reaction of SD I at pH values of 3, 4, and 5 are 0.026 2, 0.024 4, and 0.019 1 min^{-1}, respectively, with half-lives of 26.66, 28.88, and 36.48 min.

To better understand the impact of pH, the pH_{ZPC} of the prepared photocatalytic material was determined to be 5.52 (Fig. 10a). When the pH of the medium is lower than the pH_{ZPC} of the catalytic material, the surface of the material is positively charged, which facilitates the migration and adsorption of SD I toward the surface of the material
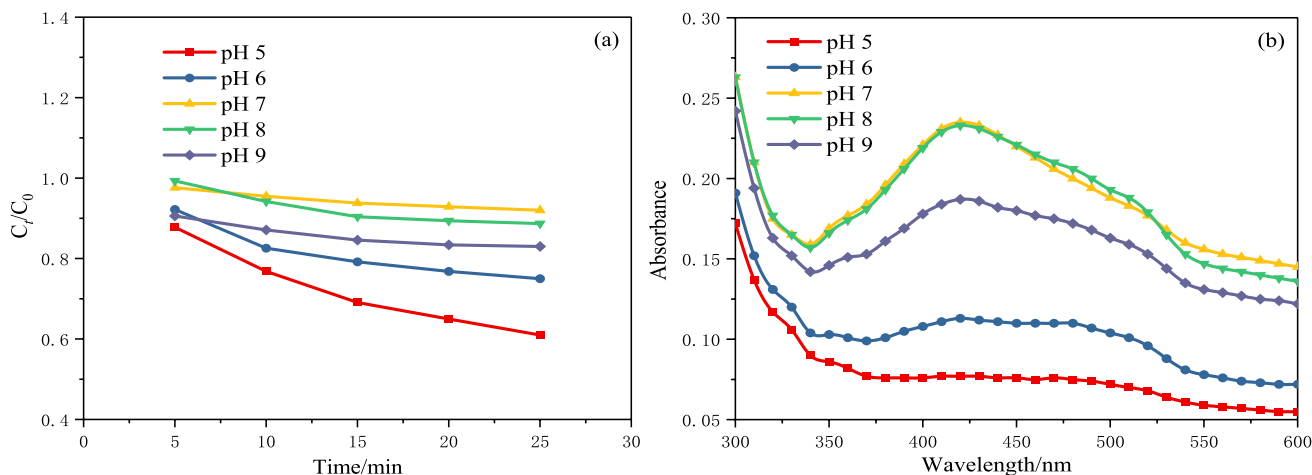

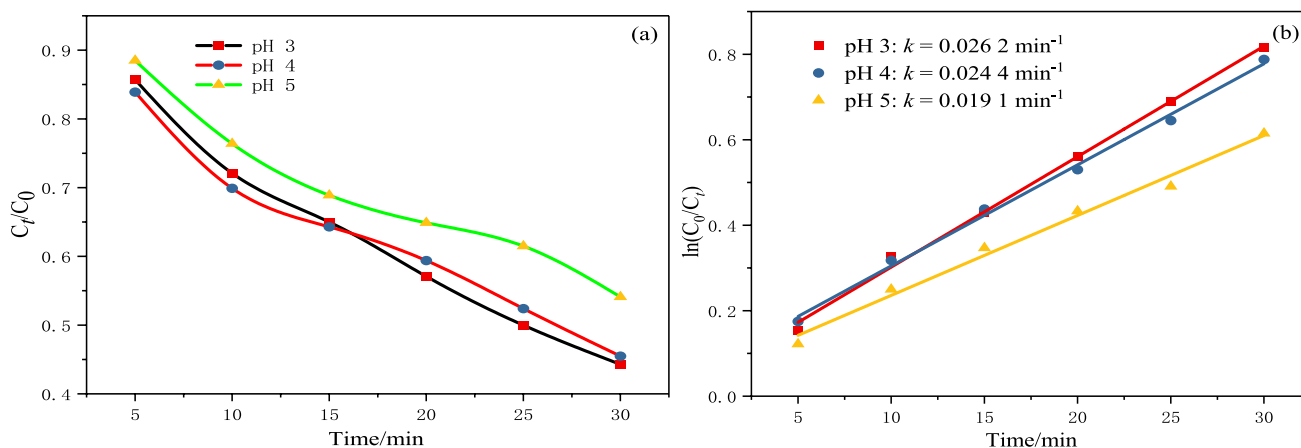**Fig. 8** Degradation efficiency (**a**) and UV–Vis spectra (**b**) of SD I at different pH

Fig. 9 Degradation efficiency (**a**) and kinetic fitting curve (**b**) of SD I under acidic conditions
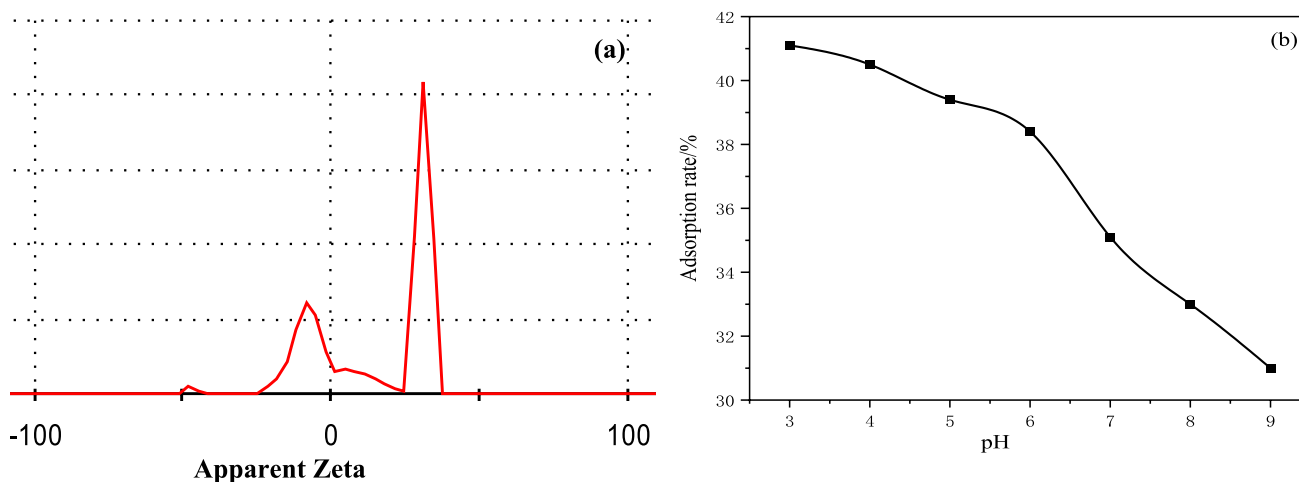
Fig. 10 pH_{ZPC} (**a**) and the adsorption rates (**b**) of the prepared material 1 with different pH values

(Fig. 10b) and also aids the migration of photogenerated electrons to the surface of the catalytic material. Hydroxyl radicals (·OH) are generated during the electron transfer process, promoting the further oxidation of the holes (h^+) produced during the reaction process, significantly enhancing the photocatalytic activity. Conversely, when the pH value of the medium is higher than the pH_{ZPC} of the material, the negatively charged surface hinders the adsorption of SD I anions on the surface of the material and the migration of photogenerated electrons, leading to a decrease in photocatalytic efficiency (Luo et al. 2008).

Effect of temperature

Considering the requirements of actual degradation, the impact of temperatures ranging from 20 °C to 40 °C on the degradation of SD I was studied (Fig. 11). The temperature effect was found to be insignificant, and there is not

a significant difference in degradation efficiency among the three temperatures, with a slightly higher efficiency observed at 20 °C (Fig. 11a). From the fitted pseudo-first-order reaction kinetics curves, it can also be observed that the k values at the three temperatures are around 0.023 0 min^{-1} (Fig. 11b). One possible reason is that the removal of SD I by the material involves adsorption prior to degradation, with lower temperatures favoring adsorption (Che et al. 2019). Due to the high adsorption capacity of SA and GO in the composite photocatalytic material, the adsorption rates at the three temperatures are relatively high, with the adsorption rate at 20 °C being 43.7%, while the rates at 30 °C and 40 °C are 39.44% and 38.62%, respectively. As temperature increases, the movement of SD I molecules accelerates, which is unfavorable for adsorption and degradation of SD I. Therefore, the photocatalytic degradation of SD I can be effectively carried out at lower temperatures, eliminating the need for additional heating
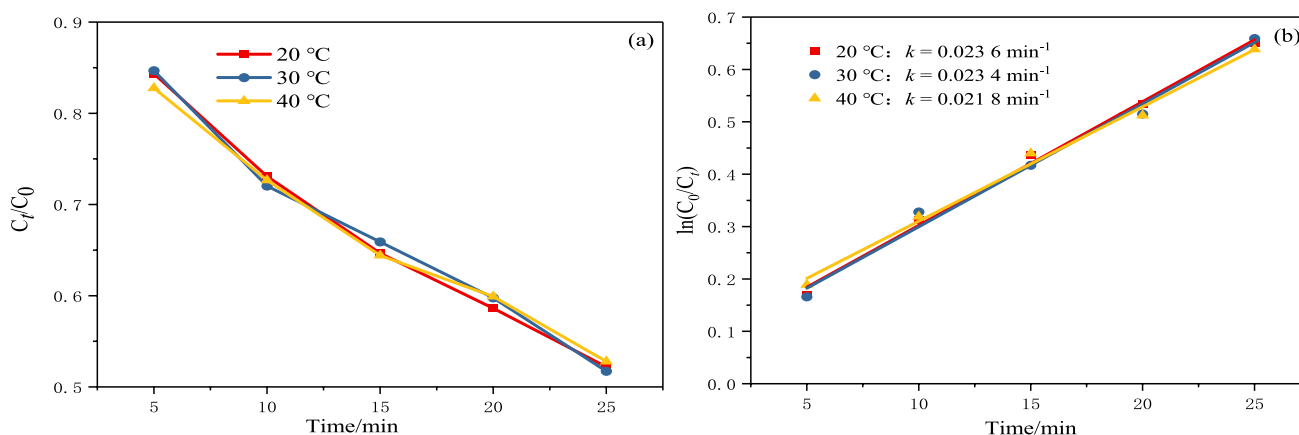

Fig. 11 Effect of different temperatures on degradation efficiency (**a**) and kinetic fitting curve (**b**)

equipment, saving energy, and facilitating catalytic reactions under sunlight.

Effects of different SD I concentrations

In general, the photocatalytic reaction rate is negatively correlated with the concentration of organic matter and positively correlated with the dosage of catalyst (Houwang et al. 2021). The preliminary test in this study demonstrated that the prepared photocatalytic material suspension of 10 mL, after centrifugation, dispersed well in 100 mL SD I solution, with good light transmittance. Based on this, the influence of the initial concentration of SD I solution (12, 10, 8, 6 mg/L) on the degradation efficiency was further investigated (Fig. 12). With the increase of the initial concentration of SD I, the degradation efficiency and k value of SD I decrease. When the initial concentration is too high, the limited adsorption sites provided by the catalyst surface can not adsorb more SD I molecules, and the SD I molecules in the solution will block the irradiation of visible light, reducing the transmittance, leading to a decrease in the utilization of visible light by the catalyst, thereby weakening the photocatalytic degradation effect (Qi et al. 2008). The optimal degradation performance of SD I is achieved when the initial concentration of SD I solution is below 10 mg/L.

Stability test of the material 1

Figure 13a shows the spectral scan of SD I (8 mg/L) degrading at pH 4. After 25 min of degradation, the absorption peak of the benzene ring structure at 305 nm in the UV region gradually disappears. In the visible region, the maximum absorption peak at 483 nm also decreases with a blue shift, changing from 483 nm to 468.5 nm. At the same time, the solution gradually turns colorless. This is due to the strong oxidative free radicals generated in the reaction
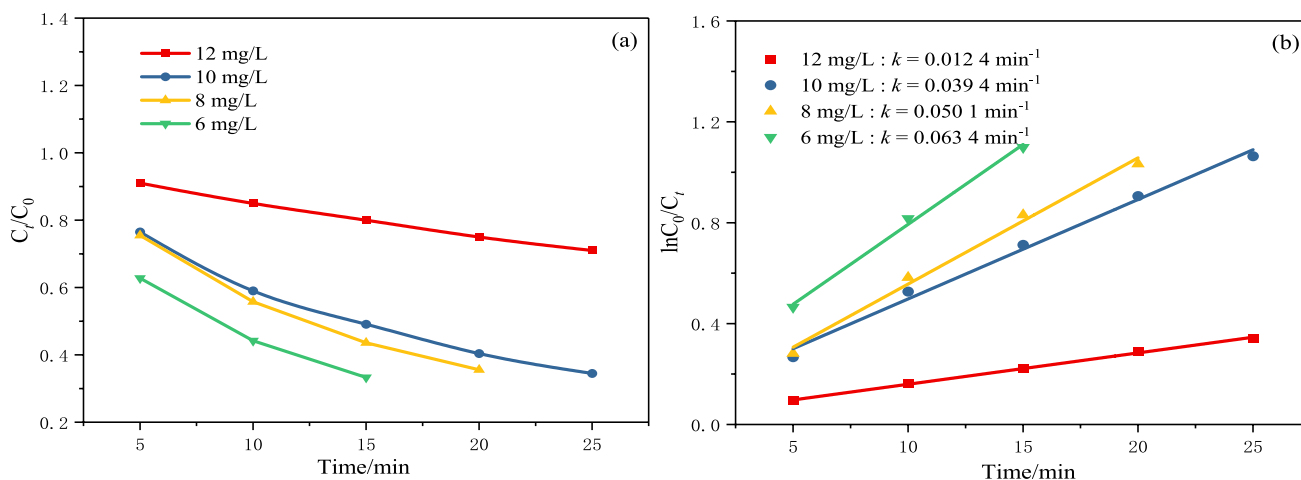

Fig. 12 Effect of different SD I concentrations on degradation efficiency (**a**) and kinetic fitting curve (**b**)
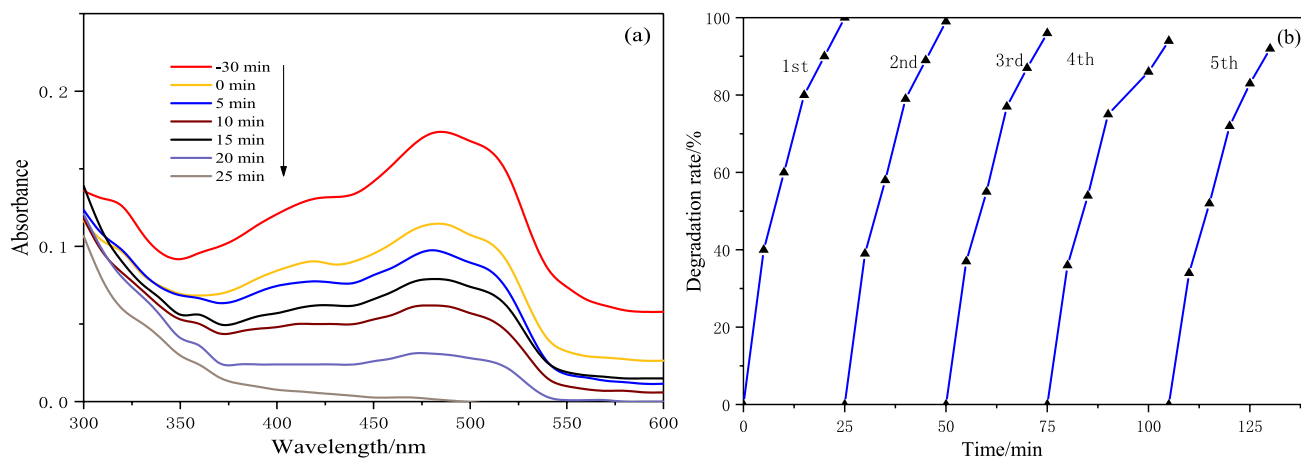

Fig. 13 Absorption spectra (**a**) of SD I degradation and stability (**b**) of cyclic degradation

system attacking the conjugated structure (chromophore) of the SD I molecule, breaking it open, and further attacks by the free radicals lead to the opening of the naphthalene and benzene ring structures, forming small molecular substances. After the material was recycled for 5 times, the degradation rate of SD I could still be maintained above 85% (Fig. 13b, indicating that the catalytic material has good photocatalytic stability。

The mechanism of photocatalytic degradation

To intuitively understand the generation of $\cdot OH$ and $\cdot O_2^-$ in the photocatalytic material 1 under light irradiation, ESR technology was used to determine the active species. In the dark, no signals of $\cdot OH$ and $\cdot O_2^-$ were detected (Fig. 14). However, after 5 and 10 min of irradiation ($\lambda > 420$ nm), characteristic quartets of $\cdot OH$ and $\cdot O_2^-$ were observed. The peak intensity ratios of the $\cdot OH$ and $\cdot O_2^-$ spectral signals were 1:2:2:1 (Fig. 14a) and 1:1:1:1 (Fig. 14b), respectively (Taborda et al. 2001).

In Fig. 15a, without the addition of quenchers, the degradation rate is 99% after 25 min. The addition of p-BQ as an $\cdot O_2^-$ quencher significantly reduced the degradation rate of SD I, with only 9.2% of SD I degraded, indicating the generation of a large amount of $\cdot O_2^-$ during the degradation of SD I by the composite material. Using EDTA-2Na as an h^+ quencher reduced the degradation rate to 48.4%, while TBA has minimal effect on the degradation of SD I.

In summary, $\cdot O_2^-$ plays a leading role in the photocatalytic degradation of SD I, followed by h^+, while $\cdot OH$ has a minor role, possibly due to the acidic conditions under which the degradation occurs leading to limited $\cdot OH$ production.

The mechanism of degradation of SD I involves the excitation of Ag_2O and AgCl under sunlight irradiation, where the corresponding photogenerated holes (h^+) and photogenerated electrons (e^-) are located in their valence band and
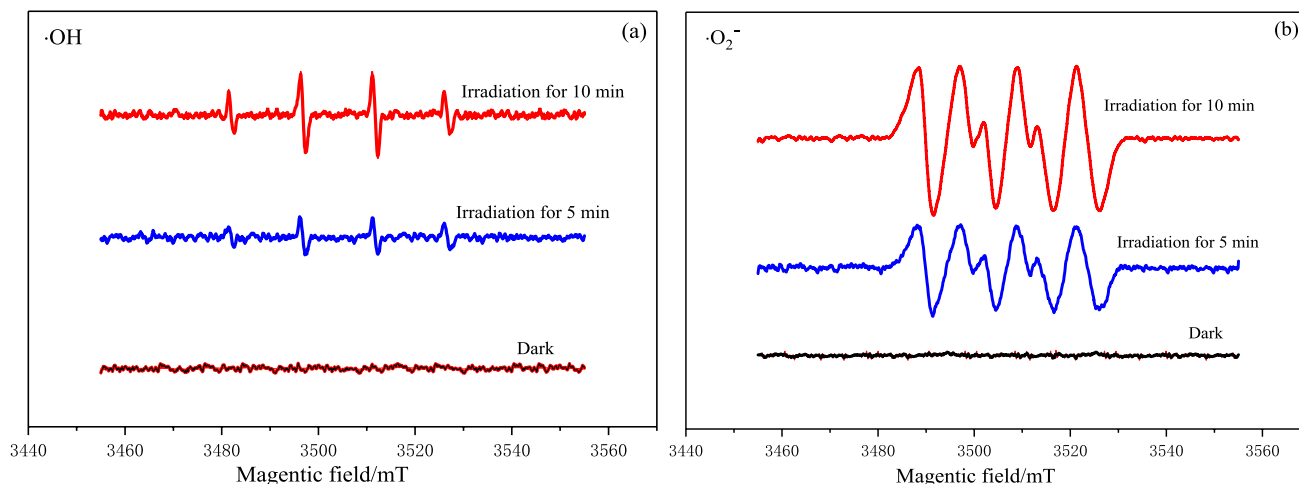

Fig. 14 ESR spectra of hydroxyl radical and superoxide radical:$\cdot OH$ (**a**) and$\cdot O_2^-$ (**b**)
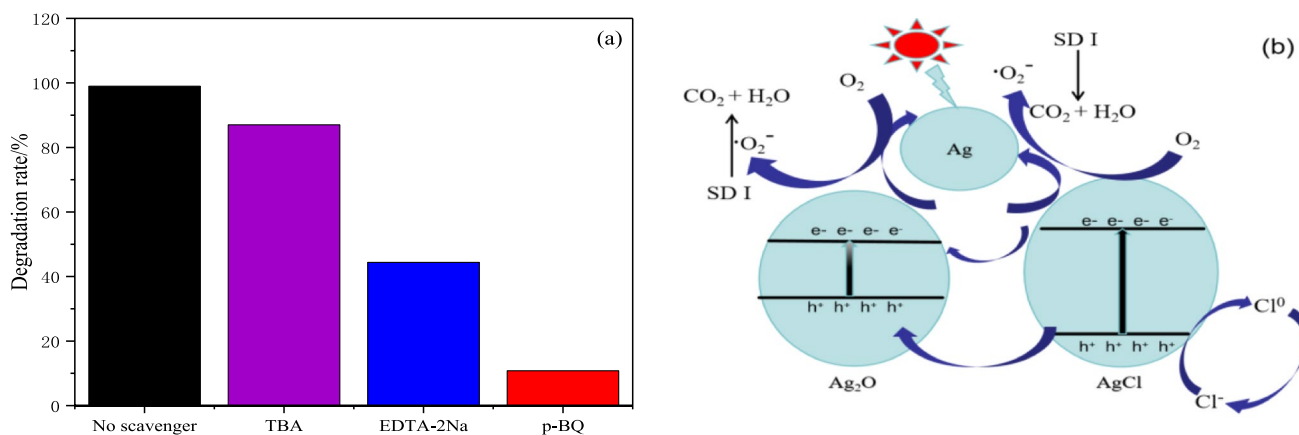

Fig. 15 Degradation rate (**a**) of SD I with different quenchers and the degradation processes (**b**) of SD I with the material 1

conduction band, respectively (Fig. 15b). Due to the SPR effect of AgNPs, the light-generated electrons are captured by AgNPs and transferred to the material surface, where they are then captured by O_2 in the solution, forming a large number of reactive oxygen species $\cdot O_2^-$. Since the valence band potential of AgCl is higher than that of Ag_2O, the holes in the valence band of AgCl can be transferred to the valence band of Ag_2O. These active groups (h^+, $\cdot O_2^-$) exhibit strong oxidizing properties, enhancing the photocatalytic performance of the composite material. In addition, some holes in the AgCl valence band can react with AgCl to produce Ag^+ and Cl^0. Cl^0 has strong oxidizing properties, causing the degradation of SD I and itself transforming into Cl^-. Cl^- then reacts with Ag^+ to reform AgCl (Huimin et al. 2023; Xing et al. 2021).

Photocatalytic degradation pathway of SD I

Based on the fragment information generated by mass spectrometry (MS) (Table 2), the possible pathways for SD I photocatalytic degradation are shown in Fig. 16. SD I molecules are adsorbed onto the surface of photocatalytic materials. Under the action of holes and highly oxidative free radicals generated by light excitation, the azo molecules undergo decolorization, ring-opening of the benzene, and naphthalene rings, ultimately mineralizing into CO_2, H_2O, and inorganic ions. The N=N bonds of SD I molecules are easily sensitized and undergo electronic transition during the photocatalytic process, thereby activating the local structure of the azo molecules, making the carbon atom connected to the N=N bonds unstable. This carbon atom becomes a site for attack by strong oxidative free radicals, leading to the oxidative cleavage of the N=N bonds and the C–N bonds connected to the naphthol ring, resulting in degradation to form phenol and 1, 2-naphthoquinone (or 2-naphthalene). Phenol undergoes ring-opening to form maleic anhydride and succinic anhydride, while 1, 2-naphthoquinone, under attack by strong oxidative free radicals, forms various structural substances such as benzoic acid and phthalic acid, which are further transformed into hydroxypyruvic acid and continue to break down into small molecules and CO_2, H_2O.

Conclusions

The prepared composite catalytic material is loaded with a large amount of irregular nano-Ag_2O, AgCl, and AgNPs, with particles of different sizes showing an uneven distribution. The photocatalytic material exhibits significant absorption in both the UV and visible light regions, with a wide absorption range. Under visible light irradiation, the photocatalytic material can generate a stable and reversible photocurrent, with a small resistance to charge transfer of photogenerated electrons, demonstrating good photocatalytic performance.

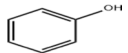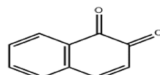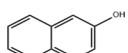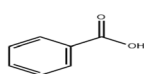**Table 2** Intermediate products of photocatalytic degradation of SD I
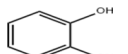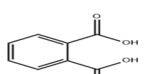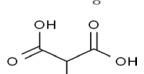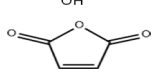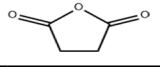
Compounds	Structural formula	m/z	Irradiation time/min			
			5	10	15	20
Phenol		94	√			
1,2-naphthalenedione		158	√	√		
2-naphthol		144	√	√		
Benzoic acid		121	√	√	√	
1,2-benzenediol		110	√	√		
Phthalic acid		166	√	√	√	√
Tartronic acid		119	√	√	√	√
Maleic anhydride		97	√	√	√	√
Succinic anhydride		99	√	√	√	√

Fig. 16 Photocatalytic degradation possible pathways of SD I
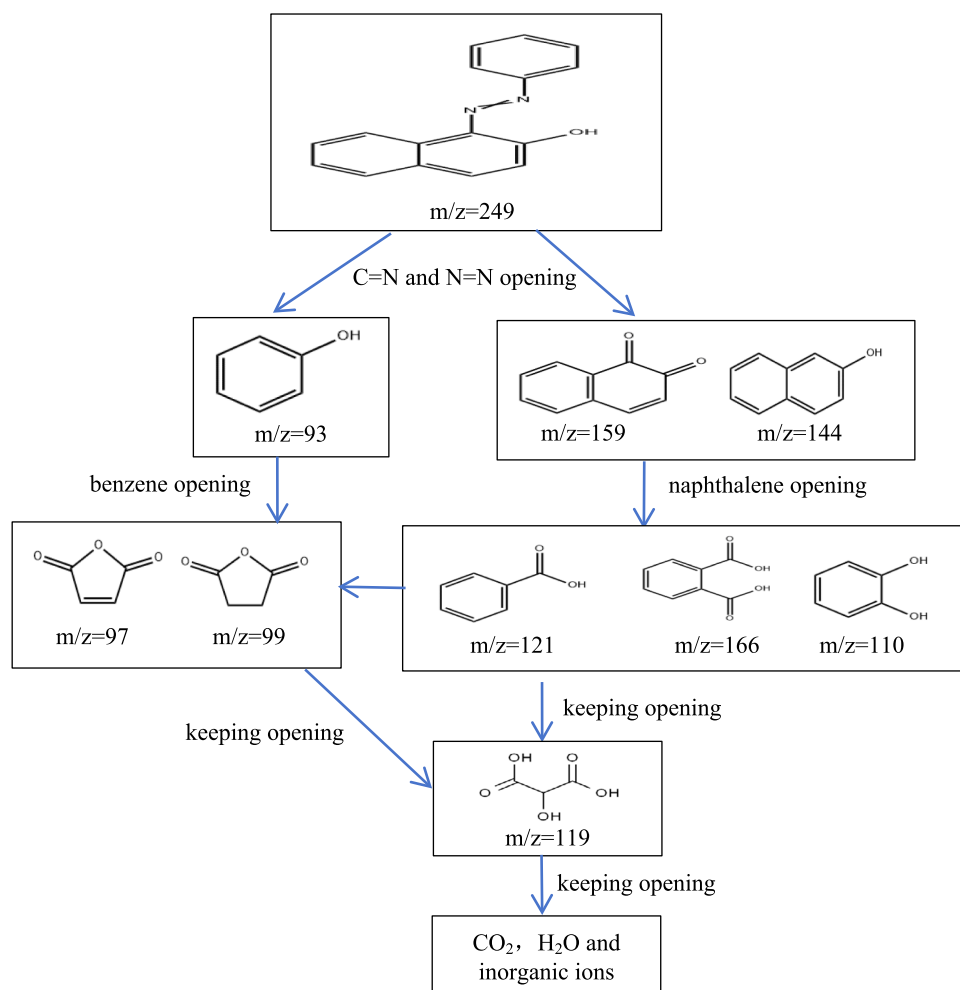
After being treated with ultrasound and heating (100 ℃) for 30 min in an APG (7 mL/1000 mL) aqueous solution, SD I exhibits good solubility, which is significantly influenced by the amount of APG added and the heating temperature. The prepared composite photocatalytic material has strong adsorption capacity and demonstrates good stability and strong catalytic degradation ability for SD I under sunlight. Acidic solutions and lower temperatures are favorable for the photocatalytic degradation of SD I, and the degradation process follows a pseudo-first-order reaction kinetics equation. Under the conditions of an initial mass concentration of SD I at 8 mg/L, an initial pH 4, and a reaction temperature of 30 ℃, SD I can be completely removed after 25 min of sunlight irradiation. During the photocatalytic degradation process, $\cdot O_2^-$ and h^+ are the main active species responsible for the degradation of SD I, and SD I molecules were finally mineralized into CO_2, H_2O, and inorganic ions.

Declarations

Conflict of interest We declare that we have no conflict of interest.

Ethical approval This article does not contain any studies with human participants or animals performed by any of the authors.

Informed consent In this article, no patient care was involved.

References

Anqi Ou, Jie L, Hailin C et al (2022) Preparation of Ag@AgCl modified $Bi_4Ti_3O_{12}$ and its visible light catalytic performance. Acta Materiae Compositae Sinica 39(4):1648–1656 (**in Chinese**)

Bi Y, Ouyang S, Cao J et al (2011) Facile synthesis of rhombic dodecahedral AgX/Ag_3PO_4(X = Cl, Br, I) heterocrystals with enhanced photocatalytic properties and stabilities. Phys Chem Chem Phys 13:10071–10075

Cao WG, Zhai KF, Zhou F (2011) UV-Vis spectra of Sudan I in ethanol solution. Chin J Spectroscopy Lab 28(03):1026–1030

Che CB, Zuo JL, Li JS et al (2019) Study of absorption of Sudan red I from aqueous solution with modified multi-walled carbon nanotubes. Appl Energy Technol 09:1–4

Chen GD, Sun M, Wei Q (2013) Ag_3PO_4/graphene-oxide composite with remarkably enhanced visible-light-driven photocatalytic activity toward dyes in water. J Hazard Mater 244–245:86–93

Eteng OE, Moses CA, Ugwor EI et al (2021) Ingestion of Sudan IV-adulterated palm oil impairs hepato-renal functions and induces the overexpression of pro-inflammatory cytokines: a sub-acute murine model. Egypt J Basic Appl Sci 9(1):11–22

Gao G, Pan M, Vecitis CD (2015) Effect of the oxidation approach on carbon nanotube surface functional groups and electrooxidative filtration performance. J Mater Chem A 3(14):7575–7582

Gao QJ, Wang X, Wang HX et al (2019) Sulfhydryl-modified sodium alginate film for lead-ion adsorption. Mater Lett 254(25):149–153

Ghaly HA, EL-Kalliny AS, GAD-Allah TA et al (2017) Stable plasmonic Ag/AgCl-polyaniline photoactive composite for degradation of organic contaminants under solar light. RSC Adv 7(21):12726–12736

Gopalan AI, Lee JC, Saianand G et al (2020) Recent progress in the abatement of hazardous pollutants using photocatalytic TiO_2-based building materials. Nanomaterials 10(9):1854

Gu S, Liu X, Wang H, et al (2022) Preparation and characterization of TiO_2 photocatalytic composites supported by blast furnace slag fibres for wastewater Degradation. Ceramics Int 0272–8842

Houwang C, Hong L, Peng Z et al (2021) Preparation of Ag_3PO_4/AgI photocatalyst and its mechanism of AMA degradation. ChemicalIndustry Eng Progress 40(08):4268–4277

Huimin Z, Fengying L, Yanqing D et al (2023) Preparation of Ag@AgCl/TiO_2/GO photocatalyst and Its photocatalytic performance. Ind Catal 31(5):36–41

Keshavulu M, Sreedhar P, Vijay Kumar P et al (2023) Synthesis and characterization of NiO-Bi_2O_3 nanocomposite material for effective photodegradation of the dyes and agricultural soil pollutants. Mater Sci Semiconductor Process 160:107432

Keshavulu M, Ranjith K, Yadagiri B et al (2024) Ag-Li-ZnO nanostructures for efficient photocatalytic degradation of organic dyes and textile wastewater under visible light treatment. J Mol Struct 1305:137750

Khan MH, Saleem Z, Ahmad M et al (2020) Hyperspectral imaging for color adulteration detection in red chili. Appl Sci Basel 10(17):5955

Li J, Zhang M, Guan Z et al (2017) Synergistic effect of surface and bulk single-electron-trapped oxygen vacancy of TiO_2 in the photocatalytic reduction of CO_2. Appl Catal B:environ 206:300–307

Li YK, Zhang DQ, Niu XJ et al (2020a) Visible-light photocatalytic activity of all inorganic halogenated perovskite composite. New Chem Mater 48(06):283–287

Li SY, Zhang M, Qu ZH (2020b) fabrication of highly active Z-scheme Ag/g-C_3N_4-Ag-Ag_3PO_4(110) photocatalyst photocatalyst for visible light photocatalytic degradation of levofloxacin with simultaneous hydrogen production. Chem Eng J 382(1):122394

Liu WB, Deng J, Zhao YB et al (2009) Preparation, spectral analysis and photocatalytic activities of TiO_2 films codoped with iron and nitrogen. Spectroscopy Spectral Anal 29(05):1394–1397

Luo H, Chen JX, Jia ZB, et al (2008) Investigation of photocatalytic degradation of Sudan III with nanometer TiO_2. Guangdong Chem Ind (08): 15–17 + 21.

Pan H, Feng J, Cerniglia CE et al (2011) Effects of orange II and Sudan III azo dyes and their metabolites on staphylococcus aureus. J Ind Microbiol Biotechnol 38:1729–1738

Qi X, Jiang Z, Chong X et al (2008) Solar photocatalytic degradation of methylene blue in carbon-doped TiO_2 nanoparticles suspension. Sol Energy 82(8):706–713

Qi YZ, Chen YT, Zhang SY et al (2015) Study on electrochemical degradation process for Sudan I based on FTO glass. Anal Test Tech Instrum 21(01):7–11

Qianqian Ke, Haizhou C, Biao H et al (2020) Preparation and photocatalytic performance of Ag/AgCl/MoO_3 compositess. J Mater Sci Eng 38(02):238–244

Qin L, Guo MQ, Liu Y (2018) Enhanced methane conversion in chemical looping partial oxidation systems using a copper doping modification. Appl Catal B:environ 235:143–149

Ramesh G, Jakeer A, Kalyana LY et al (2018) Photodegradation of organic dyes and industrial wastewater in the presence of layer-type perovskite materials under visible light irradiation. J Environ Chem Eng 6(4):4504–4513

Ren H, Jia S, Songhai W et al (2015) Phase transformation synthesis of novel Ag_2O/Ag_2CO_3/g-C_3N_4 composite with enhanced photocatalytic activity. Mater Lett 142:15–18

Shi H, Chen J, Li G et al (2013) Synthesis and characterization of novel plasmonic Ag/AgX-CNTs (X=Cl, Br, I) nanocomposite photocatalysts and synergetic degradation of organic pollutant under visible light. ACS Appl Mater Interfaces 5(15):6959–6967

Shi B, Yin H, Gong J et al (2017) A novel p-nheterojunction of Ag_2O/$Bi_4T_{i3}O_{12}$ nanosheet with exposed (001) facets for enhanced visible-light-driven photocatalytic activity. Mater Lett 201:74–77

Song D, Park SJ, Kang HW et al (2013) Recovery of lithium(I), strontium(II), and lanthanum(III) using Ca–alginate beads. J Chem Eng Data 58(9):2455–2464

Sun LL, Liu CY, Li JZ et al (2019) Fast electron transfer and enhanced visible light photocatalytic activity by using poly-o-phenylenediamine modified AgCl/g-C_3N_4 nanosheets. Chin J Catal 40(3):80–94

Sun D, Zhang Y, Liu YF et al (2020) In-situ homodispersely immobilization of Ag@AgCl on chloridized g-C_3N_4 nanosheets as an ultrastable plasmonic photocatalyst. Chem Eng J 384:123259

Taborda AV, Brusa MA, Grela MA (2001) P photocatalytic degradation of phthalic acid on TiO_2 nanoparticles. Appl Catal A 208(1–2):419–426

Wang DJ, Gue L, Fu F et al (2010) Photocatalytic degradation of Sudan III in nanometer TiO_2 as photocatalys. J Anhui Agric Sci 38(07):3654–3656

Waterhouse GIN, Metson JB, Graham A (2007) Synthesis, vibrational spectra and thermal stability of Ag_3O_4 and related Ag_7O_8X salts. Polyhedron 26(13):3310

Xia T, Wallenmeyer P, Anderson A et al (2014) Hydrogenated black ZnO nanoparticles with enhanced photocatalytic performance. RSC Adv 4(78):41654–41658

Xiao W, Yao CZ, Yang XQ (2016) Study on the biodegradation of polyglycoside surfactants. Textile Auxiliaries 33(08):13–16

Xiao JQ, Lin KS, Yu Y (2018) Novel Ag@AgClAgBr heterostructured nanotubes as high-performance visible-light photocatalysts for decomposition of dyes. Catal Today 314:10–19

Wang Xing, Mou Kequan, Yuan Fang, et al (2021) Synthesis of Ag/Ag_2O and research visible photocatalytic properties. Appl Chem Ind 50(11): 3036–3039 + 3043

Xiu ZL, Wua YZ, Hao XP et al (2014) Graphene oxide wrapped Ag$_3$PO$_4$ sub-microparticles with highly enhanced photocatalytic activity and stability under visible light irra-diation. Mater Res Bull 59:192–198

Yang S, Xua D, Chen B et al (2016) Synthesis and visible-light-driven photocatalytic activity of p-n heterojunction Ag$_2$O/NaTaO$_3$ nanocubes. Appl Surface Sci 383:214–221

Yang J, Li L, Fu F et al (2023) Construction of Z-scheme Ag/AgCl/Bi$_2$WO$_6$ photocatalysts with enhanced visiblelight photocatalytic performance for gaseous toluene degradation. Appl Surf Sci 610:155598

Zhang JP (2009) The spectral properties and electrolyzation of Sudan. Chang 'an University

Zhang XX, Liang SY, Hu X (2023) One-stop detection of Sudan I based on combined technology. Guangdong Public Secur Sci Technol 31(03):31–34

Zhao M, Yuan Q, Zhang H et al (2019) Synergy of adsorption and photocatalysis on removal of high-concentration dye by Ag/AgCl/Bi$_6$O$_4$(OH)$_4$(NO$_3$)6·H$_2$O nanocomposite using Bi$_{12}$O$_{17}$Cl$_2$ as bismuth source. J Alloy Compd 782:1049–1057